Optical wall dynamics induced by coexistence of monostable and bistable spatial regions

V. Odent,[1,2,*] E. Louvergneaux,[1] M. G. Clerc,[2,†] and I. Andrade-Silva[2]

[1]*Univ. Lille, CNRS, UMR 8523 - PhLAM - Physique des Lasers Atomes et Molécules, F-59000 Lille, France*
[2]*Departamento de Física, Facultad de Ciencias Físicas y Matemáticas, Universidad de Chile, Casilla 487-3, Santiago, Chile*

When nonequilibrium extended homogeneous systems exhibit multistability, it leads to the presence of domain walls between the existing equilibria. Depending on the stability of the steady states, the dynamics differs. Here, we consider the interface dynamics in the case of a spatially inhomogeneous system, namely, an optical system where the control parameter is spatially Gaussian. Then interfaces connect the *monostable* and the *bistable nonuniform states* that are associated with two distinct spatial regions. The coexistence of these two regions of different stability induces relaxation dynamics and the propagation of a wall with a time-dependent speed. We emphasize analytically these two dynamical behaviors using a generic bistable model. Experimentally, an inhomogeneous Gaussian light beam traveling through either a dye-doped liquid crystal cell or a Kerr cavity depicts these behaviors, in agreement with the theoretical predictions.

I. INTRODUCTION

Macroscopic systems under the influence of injection and dissipation of quantities such as energy, momenta, and matter usually exhibit a coexistence of different states, denoted as multistability [1,2]. This is clearly a nonlinear nature manifestation of systems far from equilibrium. Initial heterogeneous conditions initially caused by the inherent fluctuations generate spatial domains that are separated by their respective interfaces. These interfaces are known as front solutions, interfaces, domain walls, or wave fronts [2–4], depending on the physical context where they are considered. Interfaces between these metastable states appear in the form of propagating fronts and give rise to rich spatiotemporal dynamics [5–7]. Front dynamics occurs in systems as varied as walls separating magnetic domains [8], directed solidification processes [9], nonlinear optical systems [10–13], oscillating chemical reactions [14], fluidized granular media [15–21], and population dynamics [22–24], to mention a few.

From the point of view of dynamical systems theory, in one spatial dimension, a front is a nonlinear solution that is identified in the comoving frame system as a heteroclinic orbit linking two spatially extended uniform states [25,26]. The evolution of front solutions can be regarded as a particle-type one, i.e., they can be characterized by a set of continuous parameters such as position, core width, and so forth. The interface dynamics depends on the nature of the steady states that are connected. In the case of a front connecting a stable and an unstable uniform state, it is usually called a Fisher-Kolmogorov-Petrovsky-Piskunov (FKPP) front [22,27,28]. One of the main features of these fronts is that their propagating speed is not unique but determined by the initial conditions. When the initial condition is bounded, after a transient state, two counterpropagative fronts with the minimum asymptotic velocity emerge [22,27,28]. FKPP fronts have been observed in Taylor-Couette [29], Rayleigh-Bénard experiments [30], pearling and pinching on the propagating Rayleigh instability [31], spinodal decomposition in polymer mixtures [32], and

liquid crystal light valves [12]. The former scenario changes drastically when the front connects two stable uniform states. In this case, a variational system tends to develop the most stable state with a well-defined unique velocity, in order to minimize its energy or Lyapunov function, so that the front solution always propagates towards the most energetically unfavorable steady state. There is only one point in the parameter space for which the front is motionless, which is commonly called the Maxwell point, and is the point for which the two states have exactly the same energy [33]. Close to the Maxwell point, based on the parameter variation method, one can analytically determine the front velocity [5]. For variational systems away from the Maxwell point, one can have implicit expressions for the front velocity [5] that correspond to nonlinear eigenvalue problems. In the nonvariational case, the analytical expression of the front velocity is a problem still unresolved.

Thus, the dynamics of interfaces is thus rather well known for ideal systems, namely, homogeneous ones. However, many spatially physical systems do not fulfill this condition. On the contrary, the inhomogeneity can be rather important. This is the case, for instance, for optical systems involving laser beams where the amplitude profile follows a Gaussian shape. The question then arises as to the interface and its dynamics in the case of a spatially inhomogeneous system.

The aim of this article is to investigate, theoretically and experimentally, the dynamics of interfaces in a spatially inhomogeneous system, namely, an optical system where one of the control parameters is spatially Gaussian. Interfaces connect two multistable spatial states, namely, a monostable one and a bistable one associated with two distinct spatial regions. The coexistence of these two regions of different stability induces relaxation dynamics and the propagation of a wall with a variable speed. A generic bistable variational model allows analytical characterization of the dynamical behaviors. Experimentally, an inhomogeneous Gaussian light beam illuminating either a dye-doped liquid crystal cell or a Kerr antidiffractive cavity validates the theoretical predictions.

The manuscript is organized as follows: In Sec. II the general one-dimensional (1D) model is introduced and its dynamics characterized analytically and numerically. In

---
*vincent.odent@univ-lille1.fr
†marcel@dfi.uchile.cl

particular, we characterize the relaxation dynamics and the front propagation observed in different spatial regions. In Sec. II C, the extension of this study to two spatial dimensions is presented. Section III describes and analyzes the nematic-isotropic front propagation induced by the photoisomerization process. The experimental results are also compared to theoretical findings. A Kerr antidiffractive cavity submitted to an inhomogeneous Gaussian light beam is studied in Sec. IV. The dynamics of fronts is analyzed qualitatively. We conclude in Sec. V.

II. MONO- AND BISTABLE SPATIAL MODEL

Inspired by interface dynamics reported in optical experiments [34–37], where two spatially inhomogeneous states coexist, we consider a phenomenological one-dimensional stochastic bistable model with a diffusion effect and inhomogeneous media [34–37]

$$\frac{\partial u}{\partial t} = \eta(x) + u - u^3 + \frac{\partial^2 u}{\partial x^2}, \tag{1}$$

where $u(x,t)$ is a scalar order parameter, $\{x,t\}$ stand for space and time, and $\eta(x)$ is a spatially inhomogeneous bifurcation parameter that accounts for an external forcing. Notice that Eq. (1) is a dimensionless model.

The physical meaning of the scalar field and parameters depend on the experimental setup. In a nonlinear optical cavity [36], $u(x,t)$ corresponds to the intracavity light field, while parameter η is associated with the injected field [36]. In the liquid crystal light valve with optical feedback [34,35], $u(x,t)$ accounts for molecular orientation around an equilibrium state, while η is associated with the intensity of the optical feedback. In the nematic-isotropic transition induced by photoisomerization [37], $u(x,t)$ stands for molecular order, where $u \approx 1$ and $u \approx -1$, respectively, accounts for the nematic and the isotropic phase, while η accounts for the injection field amplitude. Notice that for constant η, Eq. (1) describes an extended imperfect pitchfork bifurcation [38]. Hence, the parameter η drives the nature of the solution (monostable or bistable) of the system.

Equation (1) is variational, that is,

$$\frac{\partial u}{\partial t} = -\frac{\delta F}{\delta u}, \tag{2}$$

where

$$F[u, \partial_x u] = \int \left(-\eta(x)u - \frac{u^2}{2} + \frac{u^4}{4} + \frac{(\partial_x u)^2}{2} \right) dx. \tag{3}$$

Hence, the dynamics of Eq. (1) is ruled by the minimization of F. Namely, the dynamics of this model is of relaxation.

Motivated by the front propagation induced by inhomogeneous Gaussian forcing, e.g., in dye-doped nematic liquid crystals [37], we no more consider a space independent but a spatially dependent Gaussian bifurcation parameter

$$\eta(x) = -\eta_M + \eta_0 e^{-(x/w)^2}, \tag{4}$$

where $\{\eta_M, \eta_0\}$ are constant parameters and $2w$ is the width of the Gaussian. The condition for motionless front is now local

and the Maxwell point is given by $\eta(x_M) = 0$ such that

$$|x_M| = w \sqrt{\ln\left(\frac{\eta_0}{\eta_M}\right)}. \tag{5}$$

This point corresponds to a position in space where the energy of both multistable sates are equal. As the system is variational, we can write Eq. (1) as the derivative of a potential, plus a diffusive term, by introducing the inhomogeneous potential $V(u,x)$ as

$$V(u,x) = -\eta(x)u - \frac{u^2}{2} + \frac{u^4}{4}. \tag{6}$$

The system then presents a potential which is spatially dependent. Mono- and bistable domains spatially coexist and are connected through parameter $\eta(x)$. The bistable regime is spatially located within $[x_{down}; x_{up}]$ (see Fig. 1) associated with the amplitudes $|\eta_{up/down}| = |\eta(x_{up/down})| = \pm 2/3\sqrt{3}$, such that

$$|x_{down}| = w \sqrt{\ln\left(\frac{\eta_0}{\eta_M + \eta_{down}}\right)},$$

$$|x_{up}| = w \sqrt{\ln\left(\frac{\eta_0}{\eta_M + \eta_{up}}\right)}. \tag{7}$$

The blue and green domains indicate a monostable regime outside the hysteresis cycle [Figs. 1(a) and 1(e)]. For $\eta(x) < \eta_{down}$ [respectively $\eta(x) > \eta_{up}$], the system presents a unique steady state, corresponding to $u \approx -1$ (resp. $u \approx 1$). In this regime, all the dynamics is governed by a relaxation phenomenon. Any arbitrary initial condition relaxes toward the equilibrium state with the lowest energy, as illustrated in the spatiotemporal diagrams of Figs. 1(g) and 1(k). For $\eta_{down} \leqslant \eta(x) < 0$, the system is metastable. The state $u \approx -1$ is more stable than $u \approx 1$ thanks to its lower energy, as we can see in Fig. 1(b). Considering an initial condition such that $u(x) \approx 1$, we observe front propagation, where the state $u \approx 1$ disappears in favor of the state $u \approx -1$ [Fig. 1(h)]. For $0 < \eta(x) \leqslant \eta_{up}$ the system is also metastable, but now $u \approx 1$ is the most stable steady state [Fig. 1(d)]. In this regime a front also spatially propagates [Fig. 1(j)]. In these two situations, $\eta_{dwon} \leqslant \eta(x) < \eta_{up}$, a front travels up to the location where both metastable states get the same energy, which corresponds to the Maxwell location x_M. Then the front is pinned [Figs. 1(c) and 1(i)].

A. Relaxation phenomenon, ghost and bottleneck

We first study the interface dynamics in a single monostable regime configuration. We consider, for instance, that the only existing equilibrium is u_{up2} [Fig. 1(e)]. In this regime, we consider that initially the system lies near u_{up1} and finally relaxes to u_{up2} [Fig. 1(m)]. Hence, we can separate the dynamics initially around u_{up1} and later relaxation around u_{up2}. Assuming a slow spatial variation of the bifurcation parameter ($w \gg 1$, wide Gaussian beam with respect to front width) and neglecting the diffusive term in Eq. (1), the equation becomes space independent. Furthermore, considering perturbation of the order parameter u close to its u_{up1} value (Fig. 1) in the form
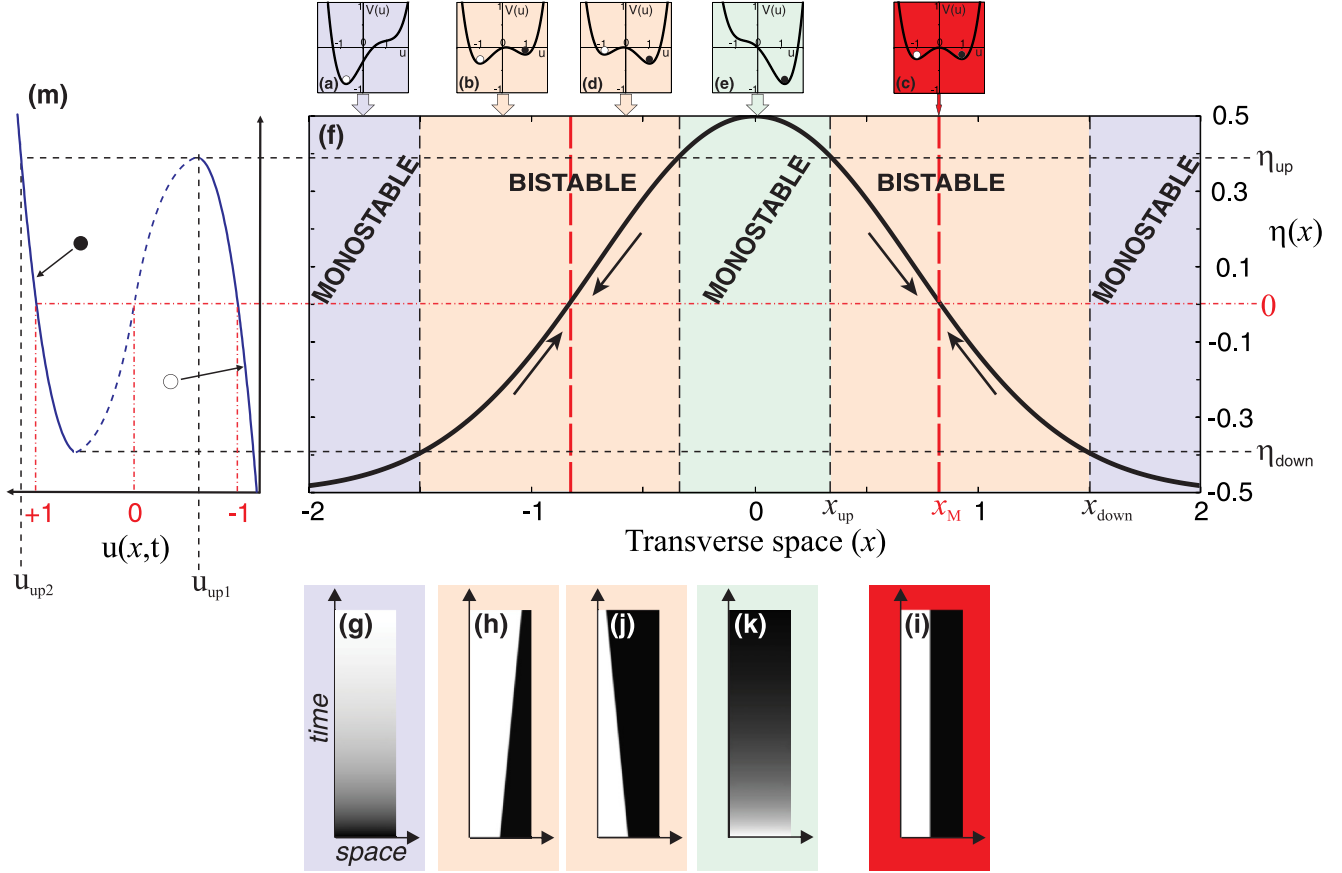
FIG. 1. (a–e) Different configurations of the potential $V(u,x)$ [Eq. (6)] versus the spatially dependent bifurcation parameter η: (a) $\eta < \eta_{\text{down}}$, (b) $\eta_{\text{down}} \leqslant \eta < 0$, (c) $\eta = 0$, (d) $0 < \eta \leqslant \eta_{\text{up}}$, and (e) $\eta_{\text{up}} < \eta$. (f) Spatial profile of $\eta(x)$, together with corresponding operating regimes (monostable or bistable). (g–k) Spatiotemporal evolution diagrams of $u(x)$ associated with the potentials $V(u,x)$ (a–e). (i) Spatiotemporal evolution diagrams of $u(x)$ at the Maxwell point, associated with the potentials $V(u,x)$ (c). (m) Hysteresis cycle for the order parameter u versus η. $\eta_0 = 1$, $\eta_M = 0.5$.

$u(x,t) \approx u_{\text{up1}} + u_1(t)$, at second order, we obtain the parabolic equation

$$\frac{du_1}{dt} = \beta + \alpha u_1^2, \tag{8}$$

with $\alpha = \sqrt{3}$ and $\beta = \eta - \eta_{\text{up}}$. This equation describes the dynamics around a saddle-node bifurcation [38]. This bifurcation occurs when β is zero ($\eta = \eta_{\text{up}}$). For β and α positive, the above equation does not possess any stationary equilibrium. The resolution of Eq. (8) gives

$$u_1(t) = \sqrt{\frac{\beta}{\alpha}} \tan[\sqrt{\alpha\beta}(t - t_0)] + u_{\text{up1}}, \tag{9}$$

where t_0 is determined by the initial conditions.

For small β, for a long time the system stays close to u_{up1}. This corresponds to a *ghost* or a *bottleneck phenomenon* [38]. One can determine the time τ spent in the bottleneck. It is given by the normalized time taken for $u_1(t)$ to go from minus to plus infinity by

$$\Gamma = \int_{-\infty}^{+\infty} \frac{du}{\alpha' - u^2}, \tag{10}$$

with $\alpha' = -\eta/\sqrt{3} + 2/9$ and $\Gamma = -\sqrt{3}\tau$. Integrating the above expression, one obtains the time spent in the vicinity of u_{up1}:

$$\tau = \frac{\pi}{\sqrt{\sqrt{3}(\eta - \eta_{\text{up}})}}. \tag{11}$$

We now can determine the relaxation time to reach u_{up2}. To find that time, we linearize the homogeneous and deterministic equation, Eq. (1), close to u_{up2}. We get

$$u_2(t) = u_{\text{up2}} - u(t_0)e^{-3(t-t_0)}, \tag{12}$$

where $t_0 \simeq \tau$ and $u(t_0)$ accounts for the initial condition. The relaxation time is $1/3$. Thus, the total relaxation time is $\tau + 1/3$. Numerical simulations of Eq. (1) confirm this analytical prediction. Figure 2 shows three different spatiotemporal evolutions for three different values of η. We observe that for a given time the system remains close to the initial conditions u_{up1} (gray state on Fig. 2) and then it transits to the black u_{up2} state. The interesting point is that this transition is spatially dependent, as we can see from Fig. 2, and is accompanied by a front dynamics. Figure 3 shows the temporal evolution of $u(t)$ taken at $x = 0$ from Fig. 2(b) (initial condition close to $u = -1$) together with the analytical expressions (9) and (12). We get a quite good agreement between the numerical
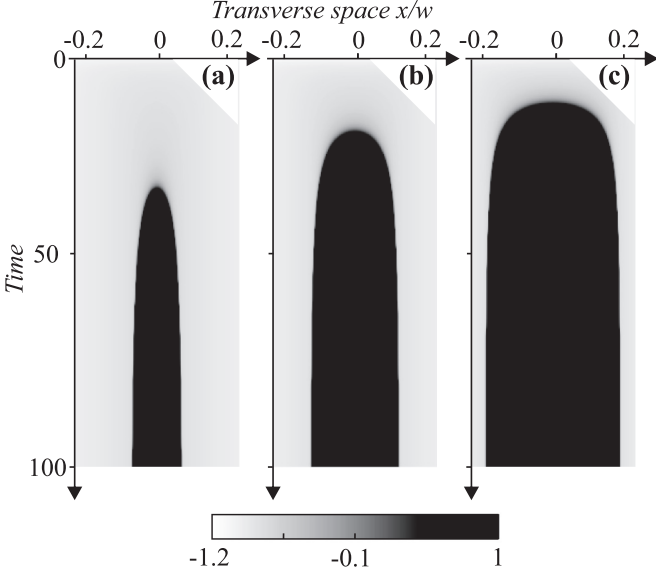
FIG. 2. Numerical spatiotemporal front propagation in the single monostable regime. From model Eq. (1) with $\eta_M = 0.5$, $w = 400$, (a) $\eta_0 = 0.89$, (b) $\eta_0 = 0.90$, and (c) $\eta_0 = 0.92$. Initial condition $u(x, t = t_0) = -1$.

simulations and the analytical predictions. To complete our analysis, we study τ evolution as a function of the bifurcation parameter η. Figure 4(a) shows the plot of time spent in the bottleneck for different η_0 values and the comparison with analytical formula (11). The agreement between numerical simulations and the theoretical prediction is excellent.

The relaxation phenomenon occurs only in the single monostable regimes (around the center of the Gaussian profile or in its wings, see Fig. 1). When the order parameter $u(x,t)$ reaches u_{up1} at $x = \pm x_{up}$ (see Fig. 1), the dynamics is governed by the bistable regime and changes completely in favor of front propagation.
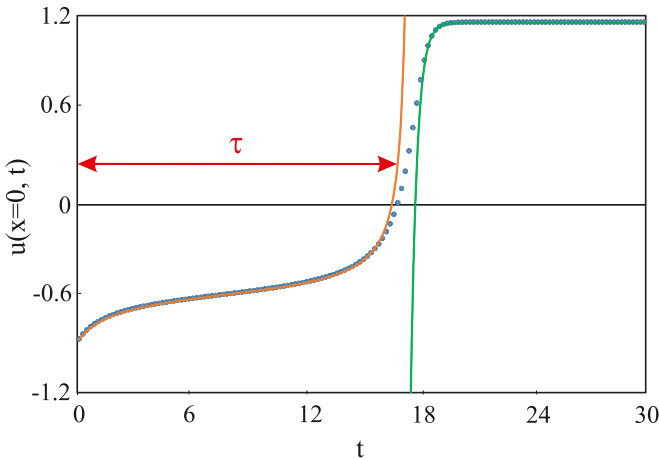

FIG. 3. Temporal evolution of $u(x = 0, t)$ from the ghost point, $u \approx -1$, to a stationary point of the monostable regime obtained from Fig. 2(b). $\eta_0 = 0.9$, $\eta_M = 0.5$, $u(t = 0) = -0.9$. • Numerical simulations, ⎯ analytical prediction for $u_1(t)$ from formula (9), and ⎯ analytical prediction for $u_2(t)$ from formula (12).
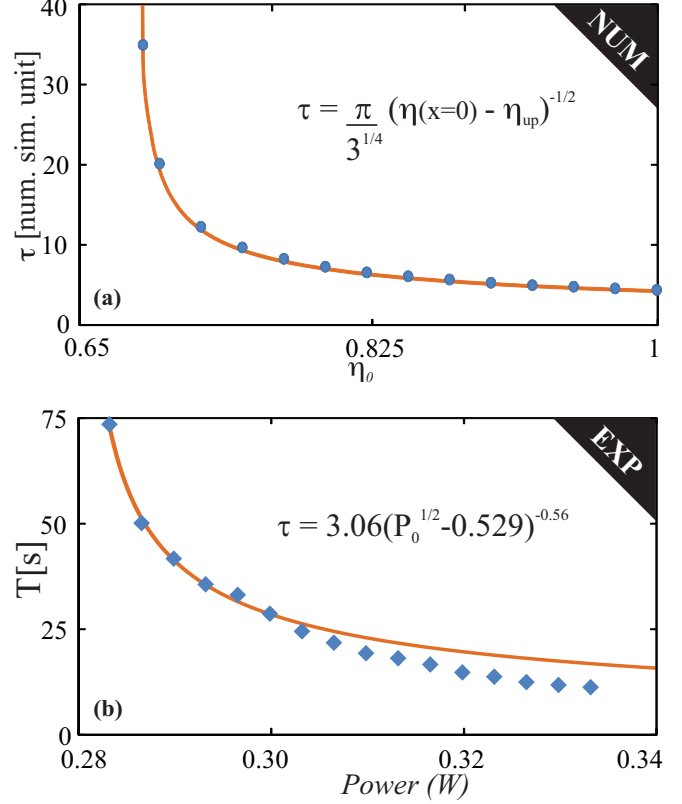

FIG. 4. Evolution of the time spent in the bottleneck versus input energy. (a) Numerical simulations; • numerical values; and ⎯ analytical prediction of nondimensional τ, measured in units of numerical simulation following relation (11); $\eta(x = 0) = \eta_0 - \eta_{Max}$; $\eta_0 = 0.9$, $\eta_M = 0.5$, $w = 200$, $u(t = 0) = -0.9$. (b) Experiments on the transition from nematic to liquid phase in dye-doped nematic liquid crystals [37]; ♦ experimental values of T in seconds and ⎯ fit on experimental points using the relation $T = m\tau$, where $m = 1.28$ is a multiplying dimension factor and τ comes from formula (11).

B. Front propagation between mono- and bistable spatial regions

When the control parameter η lies in $[\eta_{down}; \eta_{up}]$, the spatial region $[x_{up}; x_{down}]$ is bistable for the order parameter u. In this transverse domain, the wall dynamics is governed by front propagation between two stable states. To figure out the propagating front trajectory, we perform analytical development around the Maxwell point x_{Max}. In the uniform version of Eq. (1), in other words, without spatial dependence, the model Eq. (1) exhibits a motionless interface

$$u(x,t) \equiv u_h(x) = \tanh\left(\pm \frac{(x - x_0)}{\sqrt{2}}\right), \qquad (13)$$

where x_0 accounts for the position of the front core, which corresponds to the point of maximum spatial variation. In the case of a small amount of spatial variation for the bifurcation parameter, $\eta_0 \ll 1$, we can consider the following ansatz for the front solution:

$$u_h(x,t) = \tanh\left(\pm \frac{[x - x_0(t)]}{\sqrt{2}}\right) + v(x,t), \qquad (14)$$

where $x_0(t)$ is promoted to a temporal function (variation parameter method) and $v(x,t)$ is a small correction function. Introducing the above ansatz in the spatially forced model Eq. (1) and by linearizing in v one obtains

$$\mathcal{L}v = -\eta(x) - \frac{\partial u_h}{\partial x}\frac{\partial x_0}{\partial t}, \tag{15}$$

where

$$\mathcal{L} \equiv \left(1 - 3u_h^2 + \frac{\partial^2}{\partial x^2}\right)$$

is a linear operator. Introducing the inner product $\langle f|g\rangle = \int_{-\infty}^{+\infty} f\,g\,dx$, the linear operator $\mathcal{L}$ is self-adjoint ($\mathcal{L} = \mathcal{L}^+$) and $\partial_x u_h$ is the only element of the kernel of $\mathcal{L}$ which is related to the Goldstone mode of the translation invariance [2]. Hence, the above equation has a solution if the front satisfies the following solvability condition (Fredholm alternative [2]):

$$\frac{dx_0}{dt}\int_{-\infty}^{+\infty}\left(\frac{\partial u_h}{\partial x}\right)^2 dx = \int_{-\infty}^{+\infty}\frac{\partial u_h}{\partial x}\eta(x)dx. \tag{16}$$

To compute a simple expression, integrals are calculated assuming the parameter η is spatially slowly varying. This is the case close to the center of the Gaussian profile. In this region, η can be approximated to a parabola function

$$\eta(x) \approx -\eta_M + \eta_0[1 - (x/w)^2]. \tag{17}$$

After straightforward calculations, we obtain the velocity of the propagating front

$$\frac{dx_0}{dt} = -\frac{3\sqrt{2}}{2}\{-\eta_M + \eta_0[1 - (x_0/w)^2]\}. \tag{18}$$

Starting from this equation, one can infer the transverse front trajectory

$$x_0(t) = a\,\tanh[b(t - t_0)], \tag{19}$$

with $a \equiv w\sqrt{1 - \eta_M/\eta_0}$ and $b \equiv {}^3/\sqrt{2}w\sqrt{\eta_0(\eta_0 - \eta_M)}$.

The asymptotic location of the front core for an infinite time is given by

$$x_0(t \to \infty) = a = w\sqrt{1 - \frac{\eta_M}{\eta_0}}. \tag{20}$$

This expression can be also found using the first-order development of the front core location Eq. (5) for a Gaussian profile of η.

To check the validity of these analytical predictions, we perform numerical simulations of the deterministic Eq. (1) by inserting the parabolic function (17) for the bifurcation parameter η. Figure 5(b) shows the evolution of the front core location x_0 together with the corresponding associated spatiotemporal diagram of $u(x,t)$ [Fig. 5(b)]. The agreement between the numerical values of x_0 and the expression (19) is excellent.

As for a transverse Gaussian dependence for η (Fig. 2), a relaxation phenomenon is followed by a propagating front between the white and black states (Fig. 5). It is worth noting that numerical simulations of the stochastic version of Eq. (1), through the incorporation of an additional noise, evidence the same behaviors. Thus, the relaxation and front propagation phenomena are robust. The stochastic version of Eq. (1) is under investigation and the results will be published elsewhere.
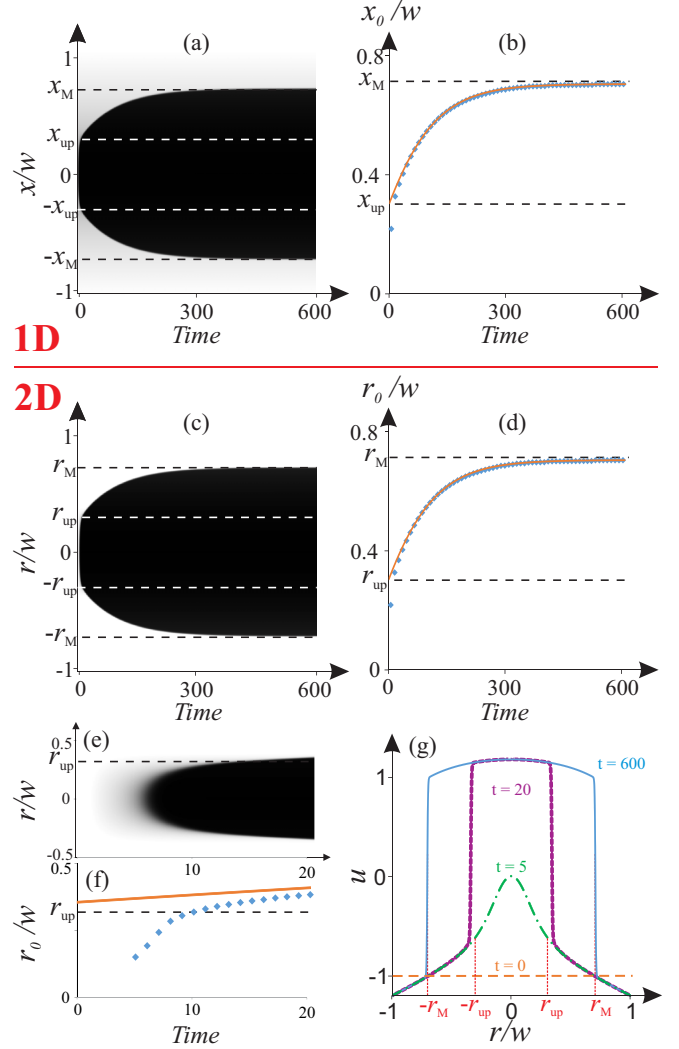

FIG. 5. 1D and 2D numerical simulations of Eqs. (1) and (21) with a parabolic forcing. (a) Spatiotemporal diagram for the 1D system, Eq. (1). (b) Front trajectory in the 1D system: ◆ numerical points, — analytical prediction from Eq. (19). (c) Spatiotemporal diagram for the 2D system, Eq. (21). (d) Front trajectory in the 2D system: ◆ numerical points, — analytical prediction from Eq. (19). (e) Spatiotemporal diagram of the relaxation phenomenon for the 2D system with (f) the front position. (g) Numerical profile of $u(r,t)$ at — $t = 0$, ·— $t = 5$, - - - $t = 20$, — $t = 600$. The parameters used for both numerical simulations are $\eta_M = 0.5$, $w = 250$, and $\eta_0 = 1$.

C. Extension to two transverse dimensions

Let us consider a natural two-dimensional (2D) extension of the 1D model Eq. (1). The mono and bistable two-dimensional spatial model reads

$$\frac{\partial u}{\partial t} = \eta(r) + u - u^3 + \nabla_\perp^2 u, \tag{21}$$

where r stands for the radial coordinate, $\{x,y\}$ accounts for the two transverse spatial Cartesian coordinates, and $\nabla_\perp^2 \equiv \partial_{xx} + \partial_{yy}$ is the two-dimensional Laplacian. Performing similar numerical simulations as for the previous 1D case, we still obtain quite good agreement between the analytical
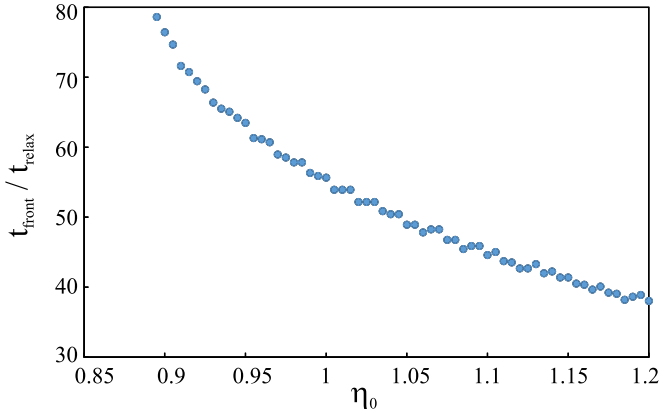
FIG. 6. Numerical comparison between the relaxation and front propagation characteristic times versus the bifurcation parameter η_0, Eq. (21); $\eta_M = 0.5$, $w = 250$.

predictions (17) and the 2D numerical simulations for the front core location r_0 when η possesses a parabolic profile [Fig. 5(d)].

A closeup of the initial temporal evolution of the order parameter u together with the interface trajectory r_0 evolution is depicted is Figs. 5(e) and 5(f), respectively. During this temporal stage ($t < 10$), the relaxation phenomenon takes place where the interface velocity is faster than those for the regime of two coexisting states. It corresponds to a location of the interface delimited by $|r| < r_{up}$, with the potential of Fig. 1(e). To illustrate the wall dynamics when the initial condition is uniform and its value is $u = -1$ but the forcing η is spatially parabolic, we plot the spatial profiles of $u(x,t)$, at different times, represented in Fig. 5(g). At $t = 0$, the initial condition is $u(x) = -1$. Between $t = 0$ and $t \sim 10$, the center part of the scalar field $u(|r| < r_{up})$ relaxes from $u = -1$ to $u = 1$. The profile of u is shown at $t = 5$. Then, two opposite fronts propagate, at $t = 20$, to reach the stationary position in r_M at $t \approx 600$.

We compared the typical time duration of the relaxation phenomenon with respect to the propagation phenomenon. The relaxation time is numerically evaluated using the time to go from the ghost state (close to u_{up1}) to the stable state (u_{up2}) for different values of η ($\eta > \eta_{up}$). The front propagation time is obtained thanks to the time taken by the front core to reach 90% of its final position x_M. Figure 6 shows the comparison between these characteristic temporal scales versus the bifurcation parameter.

To check the validity of the above theoretical predictions, we carried out two experiments: a nematic-isotropic transition induced by photoisomerization, and a focusing Kerr Fabry-Pérot cavity operating in a negative diffraction regime.

III. NEMATIC-ISOTROPIC TRANSITION INDUCED BY PHOTOISOMERIZATION

The nematic-isotropic transition is a classic problem of the theory of liquid crystals. In this transition, the nematic phase is characterized by an orientational order where molecules are mostly pointing in the same direction, unlike the isotropic liquid phase where molecules possess a random and isotropic

molecular ordering [39–41]. Therefore, as a function of temperature T, one expects to observe a transition between these two phases, that is, a critical temperature T_c corresponding to the emergence of a different ordering. Since the molecules possess a preferred orientation but not a direction, this transition is characterized by a second-rank tensor [39–41]. This tensor is a symmetric matrix with zero trace, characterized by a single scalar parameter $S(\vec{r},t)$, which is an order parameter that accounts for the alignment of the molecules. Then, when S is small (order 1) it accounts for the isotropic liquid (nematic) phase.

The dynamic of the order parameter is ruled by the free energy (Landau–de Gennes theory) [39–41]

$$\mathcal{F} = \int \left(\frac{A}{2}S^2 - \frac{B}{2}S^3 + \frac{1}{2}S^4 + \frac{(\nabla S)^2}{2} \right) dx\,dy, \quad (22)$$

where $\{A,B\}$ are phenomenological positive parameters. Usually parameter A is proportional to the temperature with respect to the critical one ($A \propto T - T_c$) [39–41]; this is the bifurcation parameter. The temporal evolution of S is characterized by the minimization of the free energy $\mathcal{F}$, that is,

$$\frac{\partial S}{\partial t} = -\frac{\delta \mathcal{F}}{\delta S} = -AS + BS^2 - S^3 + \nabla^2 S. \quad (23)$$

This model has the steady states $S = 0$ and $S \equiv S_M = (B \pm \sqrt{B^2 - 4A})/2$ that account, respectively, for the isotropic liquid and nematic phases. For large values of the bifurcation parameter ($A \gg 1$), the only supported state is the isotropic liquid phase. When the bifurcation parameter is diminished to zero ($A = 0$), the isotropic state becomes unstable through a discontinuous bifurcation (first-order transition). This bifurcation generates the emergence of the nematic state, S_M. This latter phase depicts a hysteresis (coexistence) with an isotropic state bounded by $A = 0$ to $A = B^2/4$. For negative A, the only stable state is the nematic phase.

In the case of dye-doped liquid crystal ($DDLC$) cells illuminated by a light beam, the nematic-isotropic transition can be achieved using the intensity of the beam [37,42,43] through the process of photoisomerization of dyes [37,43,44]. Hence, the parameters become a function of the intensity of the light I ($\{A(I),B(I)\}$). Then, if the light beam illuminating the sample is inhomogeneous $I(r)$, which is usually Gaussian, the parameters of the equation become inhomogeneous. Thus the equation for the order parameter reads

$$\frac{\partial S}{\partial t} = -A(r)S + B(r)S^2 - S^3 + \nabla^2 S. \quad (24)$$

Considering the change of variable $u(\vec{r},t) = S(\vec{r},t) - B(r)/3$, the above equation takes the form

$$\frac{\partial u}{\partial t} = \eta'(r) + \epsilon'(r)u - u^3 + \nabla^2 u, \quad (25)$$

with

$$\eta'(r) = \frac{AB}{3} - \frac{2B^3}{27} - \frac{\nabla^2 B}{3},$$

$$\epsilon'(r) = -A + \frac{B^2}{3}.$$

Therefore the dynamics exhibited by the order parameter of the nematic-isotropic transition induced by
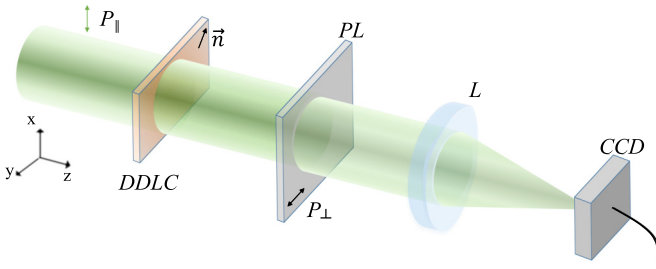
FIG. 7. Schematic sketch of the experimental setup of a nematic-isotropic transition induced by photoisomerization. DDLC: dye-doped liquid crystal illuminated by a vertically polarized laser beam ($P_\parallel$), PL: linear polarizer following the y axis ($P_\perp$), L: imaging lens, and CDD: charge-coupled device camera.

photoisomerization [37], Eq. (25), is similar to that shown by the previously phenomenological bistable model Eq. (1).

A. Experimental setup

To explore the dynamics as the result of the coexistence of mono- and bistable spatial regions, we consider the experimental setup depicted in Fig. 7. A dye-doped liquid crystal slice is subjected to a Gaussian beam illumination. The sample consists of an $E7$-oriented nematic liquid crystal layer, doped with an azo dye (methyl red, concentration $\sim0.5\%$ in weight). The mixture is injected between two polyvinyl alcohol–coated glass plates with $d = 25$-mm-thick spacers, which were rubbed to get a planar anchoring of the liquid crystal molecules (nematic director $\vec{n}$ parallel to the confining walls). The system is irradiated by a monomode frequency-doubled Nd^{3+} : $\mathrm{YVO_4}$ laser ($\lambda_0 = 532$ nm), vertically polarized (following the x axis, see Fig. 7). In the 1D configuration, we apply a symmetric spatial filtering to limit the beam size in y direction and get a quasi-1D beam ($w_x \gg w_y$). The nematic director, in the xy plane, is oriented

at 45° with respect to the input beam polarization (along the y axis). A linear polarizer PL (following the x axis) is positioned at the output of the sample, perpendicularly to the laser beam polarization. This configuration maximizes the light contrast between the two phases. The transmitted beam is monitored by a CCD camera (1280×1024 pixels). The control parameter is the beam intensity I_0 via its power P_0 and its Gaussian size w. In this experimental configuration, propagating walls between the nematic and isotropic phase that are induced by the photoisomerization process are reported [37].

B. Experimental one-dimensional nematic-isotropic wall dynamics

First, we focus our experimental work on the quasi 1D configuration. We spatially limit the beam following the y axis. Consequently, the aspect ratio (w_x/w_y) is close to 10. We apply an input laser power to initiate the photoisomerization transition. After 10 s, we observe the apparition and the expansion of the isotropic phase indicated by the black zone in Figs. 8(a) and 8(b). As a result of the light polarization and the linear polarizer PL, the nematic and isotropic phase are distinguished by having, respectively, a gray and black zone [37]. The ovoid black domain increases symmetrically following the x axis, and we can distinguish clearly the nematic phase and the isotropic liquid phase. We plot, in Fig. 8(c), a spatiotemporal diagram of the intensity profile along the dotted line to follow the wall dynamics. This diagram presents the same front dynamics than those predicted in Figs. 2 and 5(a). Furthermore, from this spatiotemporal diagram, we can infer the wall evolution as a function of time $x_0(t)$ and compare it with the theoretical prediction formula (19) of the bistable model. Figure 9 shows this comparison. Hence, experimental results show a good agreement with the one-dimensional theoretical description given by model Eq. (1). Notice that during this propagation, the walls
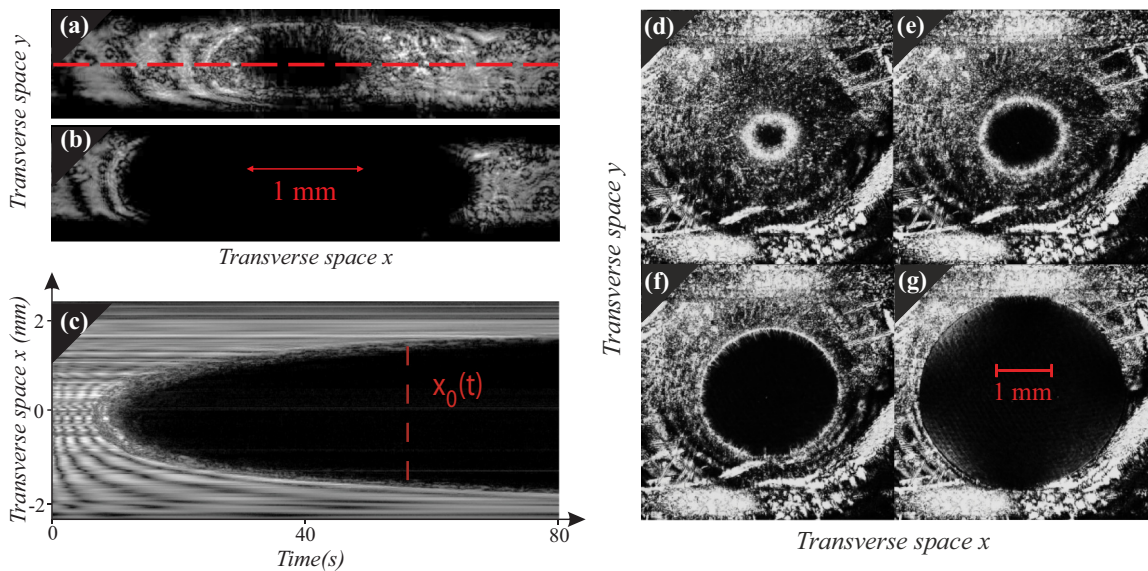

FIG. 8. Experimental nematic-isotropic front propagation. (a,b) 1D experimental snapshots for $P_0 = 2.2$ W, $w_x = 3.4$ mm, and $w_y = 0.37$ mm at 13 and 80 s, respectively. (c) Spatiotemporal diagram of the intensity profile along the dotted line on the (a) snapshot. (d–g) 2D experimental temporal sequence of snapshots for $P_0 = 350$ mW and $w_x = w_y = 3.4$ mm at 55, 65, 125, and 500 s, respectively.
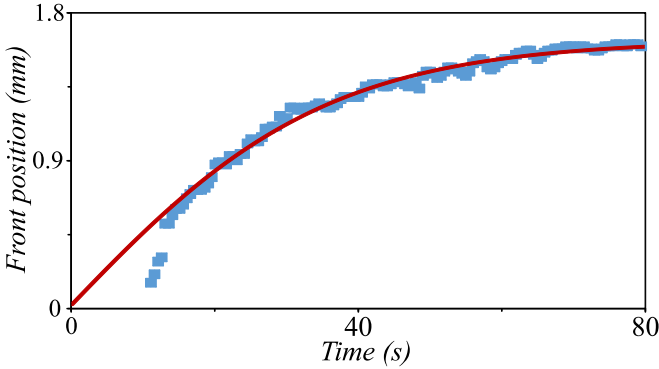
FIG. 9. Temporal wall location evolution in 1D configuration $x_0(t)$: ■ experimental points, — fit with hyperbolic tangent expression (19).
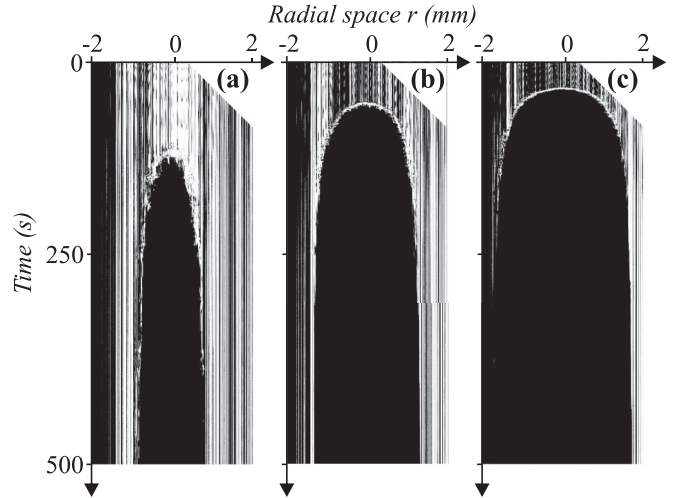

FIG. 10. One-dimensional spatiotemporal diagram of the experimental two-dimensional front propagation for three different power inputs: (a) $P_0 = 283$ mW, (b) $P_0 = 300$ mW, and (c) $P_0 = 317$ mW.

experience a decrease in velocity until they reach a stationary state. In brief, the experimental system is a quasi-one-dimensional nature and one-dimensional model, and Eq. (1) gives an adequate qualitative description of the experimental observations.

C. Experimental two-dimensional nematic-isotropic wall dynamics

We now focus on the photoisomerization process and wall propagation but in the 2D configuration. The laser beam has now a revolution symmetry with a beam radius $w = w_x = w_y$. We instantaneously increase P_0 from 5 to 350 mW. After typically 50 s, a circular wall develops in the central region of the Gaussian light beam, letting a dark disk grow [Fig. 8(d)]. The disk diameter first increases (in the transitory regime) with a decreasing velocity [Figs. 8(d)–8(f)] and then reaches a stationary value [see Fig. 8(g)]. The light intensity needed to reach the phase transition is lower for the 2D configuration with respect to the 1D configuration. The light extinction in the disk is a signature of the isotropic state, which is surrounded by the nematic phase. Notice that without any external forcing the sample is in the nematic phase at room temperature. The origin of this isotropic state is the photoisomerization process induced by light [42,43,45]. The observed wall is the result of the inhomogeneous profile of the external light beam. In the inner region of the beam the system exhibits an isotropic state due to photoisomerization, and as the power intensity decreases in the outer region the nematic state remains.

Hence, as the sample is subjected to the external beam, the isotropic state invades the nematic state until the wall stops, where the two phases are energetically equivalent, that is, at the Maxwell point. We have realized a sequence of experimental measures, where the input power is modified. For 16 input power values, between $P_0 = 283$ mW and $P_0 = 333$ mW, we record the one-dimensional spatiotemporal evolutions. From these spatiotemporal diagrams we have measured the experimental time T to observe the nematic-isotropic transition at the center of the Gaussian beam. Figure 4(b) shows T versus input power. Fitting the first eight experimental points by the formula $T = m\tau$, where $m = 1.28$ is a multiplying factor and τ comes from formula (11). Notice that m is a dimension

coefficient which takes into account the difference between the dimensionless model and the experimental data. We obtain a quite good agreement between the first experimental points and the theoretical formula.

Figure 10 shows different spatiotemporal diagrams of the experimental two-dimensional wall propagation for three different input powers. The isotropic domain extends and the response time shortens as the intensity gets higher. Also, in this case we have a quite good agreement with the numerical simulations presented in Fig. 2.

First, we focus on the response time for the system to go from the nematic phase through the isotropic phase. This study provides us with information about the onset of the bistability, characterized by η_{up} in our theoretical model. Notice that the transition between the nematic and the isotropic phase is governed by a mobile interface. At the early stage [see Fig. 8(d)] the isotropic spatial domain is small, and then its size increases versus time [Figs. 8(e)–8(g)], to reach a large extension [Fig. 8(g)]. The wall location during the early stage carries an incertitude equal to its location value, thus generating a high incertitude in the first seconds where the isotropic phase emerges. We plot the evolution of the intensity profile along a diameter of the isotropic phase black disk of Figs. 8(d)–8(g). The corresponding spatiotemporal diagram is shown in Fig. 11(a). Using the Hough transform [46], we can track the circular wall dynamics and determine its radius evolution. Figure 11(b) displays the radius evolution versus time together with the fitted analytical expression (19). Therefore the theoretical prediction exhibits an excellent agreement with experimental recordings. The first blue squares clearly evidence the occurrence of relaxation dynamics, such as described previously in Sec. II A, Eqs. (9) and (12), and numerical simulations, Fig. 5. From the above observations, we can conclude that the dynamics of a two-dimensional interface in the nematic-isotropic transition induced by photoisomerization is equally well described by the bistable model Eq. (21).
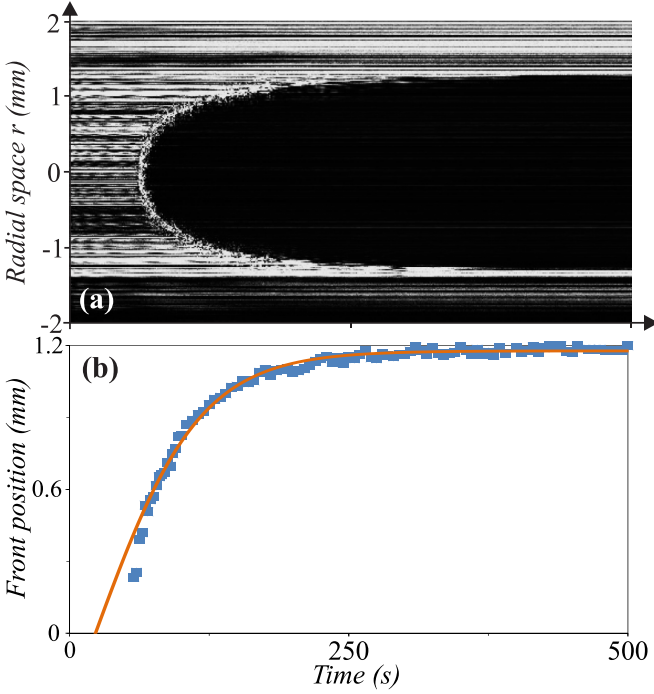
FIG. 11. (a) Experimental spatiotemporal diagram on Figs. 8(d)–8(g) taken along one black disk diameter. (b) Wall location evolution: ■ experimental points, — fit with hyperbolic tangent expression (19).

IV. EXPERIMENTAL FRONT PROPAGATION IN AN ANTIDIFFRACTIVE INHOMOGENEOUS KERR CAVITY

The passive Kerr cavity, another nonlinear optical setup, also displays wall dynamics between monostable and bistable spatial regions when it is submitted to an inhomogeneous external forcing such as a Gaussian light beam [47]. This setup presents optical bistability and is well modeled by the Lugiato-Lefever equation [48]:

$$\frac{\partial E}{\partial t} = F_0(x) - (1 + i\triangle)E + i|E|^2 E + i\alpha \frac{\partial^2 E}{\partial x^2}. \quad (26)$$

Here $E(x,t)$ is the normalized slowly varying envelope of the electric field, $\triangle$ is the detuning parameter, and $F_0(x)$ is the spatially inhomogeneous input field. As in the previous experiment, we consider a Gaussian forcing so that the input field has the form $F_0(x) = E_0 e^{-x^2/w^2}$. The envelope model, Eq. (26), is a universal model that describes a chain of coupled oscillators forced close to their natural resonant frequency, which has been derived in several physical contexts such as a plasma driven by a radio frequency field [49], a one-dimensional condensate in the presence of an applied ac field [50], and a nonlinear passive optical cavity [48].

In the positive diffraction case ($\alpha > 0$), the system exhibits pattern and soliton solutions [47,48,51,52]. In the negative diffraction case ($\alpha < 0$), the system exhibits front propagation [36,53]. Close to the critical point $\Delta = \Delta_c \equiv \sqrt{3}$, the model equation, Eq. (26), can be approximated by our phenomenological model, Eq. (1) [36]. Consequently, we expect to observe wall dynamics in the Kerr cavity submitted to an inhomogeneous Gaussian light beam forcing.
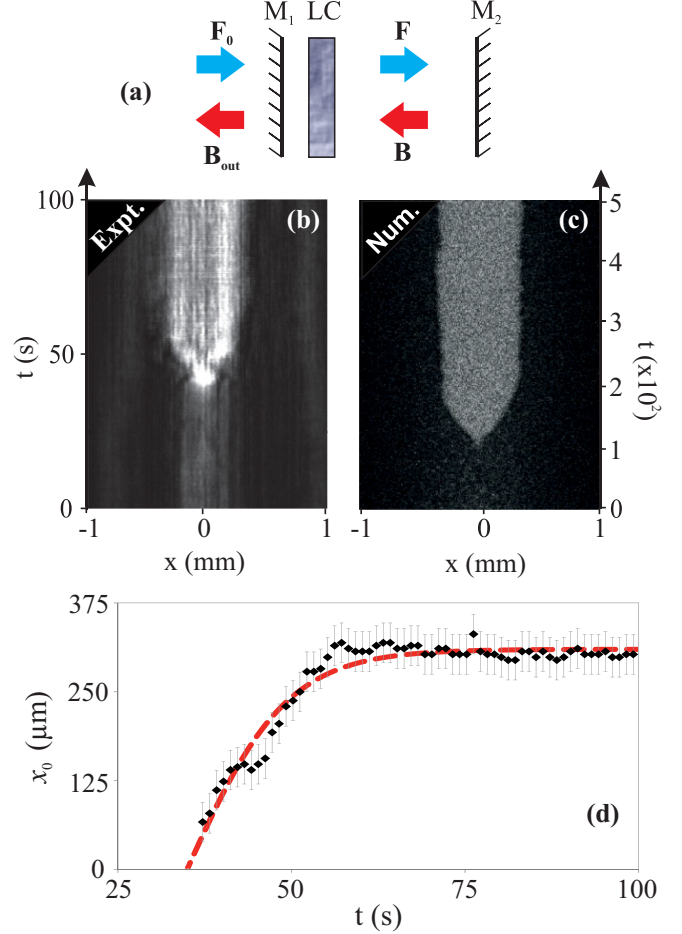

FIG. 12. Kerr cavity submitted to an inhomogeneous Gaussian light beam. (a) Schematic representation of a Kerr cavity. M_1 and M_2 are the cavity mirrors, and LC is the liquid crystal slice. (c) Experimental and (d) numerical spatiotemporal response to a step function of the input intensity from the lower (dark area) to the upper (white area) branch of the bistable cycle. Experiments $I_0 = 433\,\mathrm{W\,cm^{-2}}$, $d = -5\,\mathrm{mm}$, $\varphi = -0.6\,\mathrm{rad}$, $w_x = 1400\,\mu\mathrm{m}$, $w_y = 100\,\mu\mathrm{m}$, $R_1 = 81.8\%$; $R_2 = 81.4\%$. (b,d) Numerical simulation of model Eq. (26) with $E_0 = 1.9$, $\Delta = 3.0$, $\alpha = 0.001$, $w_x = 1400\,\mu\mathrm{m}$, $w_y = 100\,\mu\mathrm{m}$, $\varepsilon = 0.4$. (d) Wall location evolution: ♦ and dashed curve account for experimental measurements and hyperbolic tangent fit, formula (19). The experimental fit parameters are $a = 308\,\mu\mathrm{m}$, $b = 0.069$, and $t_0 = 35.2\,\mathrm{s}$.

The experiments have been carried out using a nonlinear Kerr slice medium inserted in an optical Fabry-Pérot resonator [Fig. 12(a)]. The Kerr focusing medium is a 50-μm-thick layer of $E7$ nematic liquid crystal homeotropically anchored. The cavity is delimited by two mirrors whose reflection coefficient are close to 1 ($R_1 \simeq R_2 \simeq 0.9$). The laser source, a monomode frequency-doubled Nd^{3+} : $\mathrm{YVO_4}$ laser ($\lambda_0 = 532$ nm), is used as the external inhomogeneous forcing. A more detailed description of the experimental setup is given in Refs. [47] and [36]. The middle panels of Fig. 12 show the experimental and numerical spatiotemporal diagrams of the output intensity ($|B_{out}|^2$) for a temporal step function of the input intensity. In both cases, we observe the emergence of a propagation wall connecting two different optical intensities. To characterize the

wall dynamic, we have measured experimentally its evolution as a function of time. Figure 12(d) shows wall location evolution. The wall location follows a hyperbolic tangent trajectory as predicted by our theory from Eq. (19). Hence, the interface dynamics in an antidiffractive inhomogeneous Kerr cavity is well described by the bistable model equation, Eq. (21).

V. CONCLUSION AND REMARKS

Far from equilibrium, systems usually exhibit a rich domain wall dynamics between steady states. The majority of theoretical studies consider a spatially homogeneous driven forcing. At variance, a greater number of experimental studies deal with spatially inhomogeneous driven forcing as the result of boundary conditions, inherent experimental imperfections, or the intrinsic nature of the forcing. This inhomogeneous driven forcing can induce unexpected dynamical behaviors.

We have investigated, theoretically and experimentally, the front dynamics when there is a spatial coexistence between monostable and bistable spatial regions in a simple inhomogeneous bistable variational model with either one or two transverse dimensions. This coexistence induces wall dynamics, which corresponds initially, in the monostable region, to a relaxation dynamics followed by a front propagation with a variable speed in the bistable region. From a generic bistable model, we have characterized analytically these dynamical behaviors, which are confirmed by numerical simulations. Experimentally, a dye-doped liquid crystal cell and a Kerr cavity submitted to an inhomogeneous Gaussian light beam are used to validate our theoretical predictions. The agreement between theoretical and experimental findings is fairly good.

The consideration of inhomogeneous forcing may allow dynamical control between different domains. This opens the possibility of imagining novel devices such as photo-controlled optical aperture and adaptive lenses.

[1] G. Nicolis and I. Prigogine, *Self-Organization in Nonequilibrium Systems* (John Wiley and Sons, New York, 1977).

[2] L. M. Pismen, *Patterns and Interfaces in Dissipative Dynamics*, Springer Series in Synergetics (Springer-Verlag, Berlin, Heidelberg, 2006).

[3] M. C. Cross and P. C. Hohenberg, Rev. Mod. Phys. **65**, 851 (1993).

[4] M. Cross and H. Greenside, *Pattern Formation and Dynamics in Nonequilibrium Systems* (Cambridge University Press, New York, 2009).

[5] Y. Pomeau, Physica D **23**, 3 (1986).

[6] J. S. Langer, Rev. Mod. Phys. **52**, 1 (1980).

[7] P. Collet and J. Eckman, *Instabilities and Fronts in Extended Systems,* Princeton Series in Physics (Princeton University Press, Princeton, NJ, 2014).

[8] A. H. Eschenfelder, *Magnetic Bubble Technology* (Springer, Berlin, 1980).

[9] T. Börzsönyi, S. Akamatsu, and G. Faivre, Phys. Rev. E **80**, 051601 (2009).

[10] M. G. Clerc, S. Residori, and C. S. Riera, Phys. Rev. E **63**, 060701 (2001).

[11] D. Gomila, P. Colet, G.-L. Oppo, and M. San Miguel, Phys. Rev. Lett. **87**, 194101 (2001).

[12] M. G. Clerc, T. Nagaya, A. Petrossian, S. Residori, and C. S. Riera, Eur. Phys. J. D **28**, 435 (2004).

[13] S. Residori, Phys. Rep. **416**, 201 (2005).

[14] V. Petrov, Q. Ouyang, and H. L. Swinney, Nature (London) **388**, 655 (1997).

[15] I. Aranson and L. Tsimring, *Granular Patterns* (Oxford University Press, Oxford, UK, 2008).

[16] F. Melo, P. B. Umbanhowar, and H. L. Swinney, Phys. Rev. Lett. **75**, 3838 (1995).

[17] S. Douady, S. Fauve, and C. Laroche, Europhys. Lett. **8**, 621 (1989).

[18] S. J. Moon, M. D. Shattuck, C. Bizon, D. I. Goldman, J. B.Swift, and H. L. Swinney, Phys. Rev. E **65**, 011301 (2001).

[19] S. J. Moon, D. I. Goldman, J. B. Swift, and H. L. Swinney, Phys. Rev. Lett. **91**, 134301 (2003).

[20] J. E. Macias, M. G. Clerc, C. Falcon, and M. A. Garcia-Nustes, Phys. Rev. E **88**, 020201 (2013).

[21] J. E. Macias and C. Falcon, New J. Phys. **16**, 043032 (2014).

[22] J. D. Murray, *Mathematical Biology* (Springer, Berlin, 1989).

[23] R. A. Fisher, Annals of Eugenics **7**, 355 (1937).

[24] M. G. Clerc, D. Escaff, and V. M. Kenkre, Phys. Rev. E **72**, 056217 (2005).

[25] W. van Saarloos and P. Hohenberg, Physica D **56**, 303 (1992).

[26] P. Coullet, Int. J. Bifurcation Chaos Appl. Sci. Eng. **12**, 2445 (2002).

[27] A. Kolmogorov, I. Petrovsky, and N. Piskunov, Bull. Univ. Moskou Ser. Int. Se. A **1**, 1 (1937).

[28] W. van Saarloos, Phys. Rep. **386**, 29 (2003).

[29] G. Ahlers and D. S. Cannell, Phys. Rev. Lett. **50**, 1583 (1983).

[30] J. Fineberg and V. Steinberg, Phys. Rev. Lett. **58**, 1332 (1987).

[31] T. R. Powers and R. E. Goldstein, Phys. Rev. Lett. **78**, 2555 (1997).

[32] J. Langer, An introduction to the kinetics of first-order phase transition, in *Solids Far from Equilibrium*, edited by C. Godroche (Cambridge University Press, Cambridge, UK, 1992).

[33] R. E. Goldstein, G. H. Gunaratne, L. Gil, and P. Coullet, Phys. Rev. A **43**, 6700 (1991).

[34] F. Haudin, R. G. Elias, R. G. Rojas, U. Bortolozzo, M. G. Clerc, and S. Residori, Phys. Rev. Lett. **103**, 128003 (2009).

[35] F. Haudin, R. G. Elias, R. G. Rojas, U. Bortolozzo, M. G. Clerc, and S. Residori, Phys. Rev. E **81**, 056203 (2010).

[36] V. Odent, M. Tlidi, M. G. Clerc, P. Glorieux, and E. Louvergneaux, Phys. Rev. A **90**, 011806 (2014).

[37] V. Odent, M. G. Clerc, C. Falcón, U. Bortolozzo, E. Louvergneaux, and S. Residori, Opt. Lett. **39**, 1861 (2014).

[38] S. H. Strogatz, *Nonlinear Dynamics and Chaos: With Applications to Phyics, Biology, Chemistry, and Engineering* (Westview Press, Boulder, CO, 2014).

[39] G. Vertogen and W. H. Jeu, *Thermotropic Liquid Crystals, Fundamentals* (Springer, Berlin,1988).

[40] S. Chandrasekhar, *Liquid Crystal* (Cambridge University Press, New York, 1992).

[41] P. G. de Gennes and J. Prost, *The Physics of Liquid Crystals*, International Series of Monographs on Physics (Clarendon Press, Oxford, 1995).

[42] A. Shishido, O. Tsutsumi, A. Kanazawa, T. Shiono, T. Ikeda, and N. Tamai, J. Am. Chem. Soc. **119**, 7791 (1997).

[43] I. C. Khoo, *Liquid Crystals*, 2nd ed. (John Wiley and Sons, NJ, 2007).

[44] I. Jánossy and L. Szabados, J. Nonlinear Opt. Phys. Mater. **07**, 539 (1998).

[45] I. C. Khoo, Phys. Rep. **471**, 221 (2009).

[46] D. H. Ballard, Pattern Recogn. **13**, 111 (1981).

[47] V. Odent, M. Taki, and E. Louvergneaux, New J. Phys. **13**, 113026 (2011).

[48] L. A. Lugiato and R. Lefever, Phys. Rev. Lett. **58**, 2209 (1987).

[49] G. Morales and Y. Lee, Phys. Rev. Lett. **33**, 1016 (1974).

[50] D. Kaup and A. Newell, Phys. Rev. B **18**, 5162 (1978).

[51] A. Scroggie, W. Firth, G. McDonald, M. Tlidi, R. Lefever, and L. Lugiato, Chaos, Solitons Fractals **4**, 1323 (1994), Special Issue: Nonlinear Optical Structures, Patterns, Chaos.

[52] W. J. Firth, G. K. Harkness, A. Lord, J. M. McSloy, D. Gomila, and P. Colet, J. Opt. Soc. Am. B **19**, 747 (2002).

[53] P. Tassin, G. V. der Sande, N. Veretenov, P. Kockaert, I. Veretennico, and M. Tlidi, Opt. Express **14**, 9338 (2006).